J. Fluid Mech. (2010), *vol.* 644, *pp.* 217–244.
doi:10.1017/S0022112009992217

Sliding, pinch-off and detachment of a droplet on a wall in shear flow

HANG DING†, MOHAMMAD N. H. GILANI AND PETER D. M. SPELT‡

Department of Chemical Engineering, Imperial College London SW7 2AZ, UK

(Received 16 July 2008; revised 11 September 2009; accepted 12 September 2009)

We investigate here what happens beyond the onset of motion of a droplet on a wall by the action of an imposed shear flow, accounting for inertial effects and contact-angle hysteresis. A diffuse-interface method is used for this purpose, which alleviates the shear stress singularity at a moving contact line, resulting in an effective slip length. Various flow regimes are investigated, including steadily moving drops, and partial or entire droplet entrainment. In the regime of quasi-steadily moving drops, the drop speed is found to be linear in the imposed shear rate, but to exhibit an apparent discontinuity at the onset of motion. The results also include the relation between a local maximum angle between the interface and the wall and the instantaneous value of the contact-line speed. The critical conditions for the onset of entrainment are determined for pinned as well as for moving drops. The corresponding critical capillary numbers are found to be in a rather narrow range, even for quite substantial values of a Reynolds number. The approach to breakup is then investigated in detail, including the growth of a ligament on a drop, and the reduction of the radius of a pinching neck. A model based on an energy argument is proposed to explain the results for the rate of elongation of ligaments. The paper concludes with an investigation of detachment of a hydrophobic droplet from the solid wall.

1. Introduction

In previous work it has been established that beyond a critical shear rate value, or below a critical window of contact-angle hysteresis, a droplet cannot remain at a fixed location on a wall when exposed to a shear flow. This fundamental problem in fluid mechanics has been investigated with a variety of applications in mind (with corresponding adaptations in the problem formulation), including spray coating and enhanced oil recovery (Dimitrakopoulos & Higdon 1998), fuel cells (Golpaygan & Ashgriz 2008), detergency (Chatterjee 2001), cell adhesion (see Hodges & Jensen 2002), viscous gravity currents (e.g. Eames, Gilbertson & Landeryou 2005), and is an alternative to displacing droplets by chemical inhomogeneities of the wall (Thiele & Knobloch 2006). A further motivation for the present work is to investigate for what local shear rate values droplets are displaced from a pipe wall by gas flow in oil/gas pipelines. Results for the corresponding critical value of

† Present address: Department of Chemical Engineering, University of California, Santa Barbara, CA 93106-5080, USA

‡ Email address for correspondence: p.spelt@imperial.ac.uk

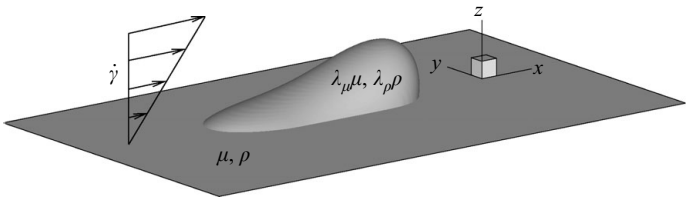

FIGURE 1. Problem definition sketch. The drop shape shown is that for a drop moving at approximately constant speed for $Re = 18$ and $Ca = 0.17$.

a capillary number $Ca = \mu\dot{\gamma}a/\sigma$ for a given window of hysteresis (or vice versa) of three-dimensional droplets have been presented by Dimitrakopoulos & Higdon (1998) and Dimitrakopoulos (2007a) for creeping flow conditions. For moderate values of a Reynolds number $Re = \rho\dot{\gamma}a^2/\mu$, the critical value of the corresponding Weber number, $We = ReCa$ was investigated by Ding & Spelt (2008). Here, ρ and μ are the density and viscosity of the surrounding fluid, respectively, a is an effective drop radius, $\dot{\gamma}$ is the imposed shear rate and σ is the surface tension coefficient (see also figure 1). In this paper, we investigate what happens beyond criticality using a numerical method.

As may be anticipated, unless the contact line remains pinned for all contact angle values, a first regime found is one wherein drops reach a quasi-steady state, such that they move eventually at constant speed, having been deformed substantially. An example of such a drop shape is given in figure 1. Several issues are investigated regarding this regime in this paper. The results will be used to confirm a conjecture by Dussan V. (1987) regarding the shape of drops moving in this flow for relatively flat drops. Secondly, we investigate the effect of initial conditions in this flow regime. Ding & Spelt (2008) found that the conditions for the onset of motion of drops (shape and critical Weber or capillary number) are affected by the initial shape of the drop. As pointed out by Dimitrakopoulos & Higdon (1998), droplets can be produced either by injecting liquid into the droplet, resulting in a spherical-cap droplet with a uniform contact angle equal to the advancing contact angle, or by subsequently withdrawing some liquid, which would yield a flatter droplet with the contact angle equal to the receding contact angle. Our previous work confirmed that the two different 'optimum' shapes determined by Dimitrakopoulos & Higdon (1998) could be approached (with some minor qualifications) by starting numerical simulations with these two different initial conditions (Ding & Spelt 2008). This motivates us here to investigate if and how the initial droplet shape affects a sliding droplet. Thirdly, we investigate to what extent a Cox–Voinov-type relation Cox (1986) can be formulated between an apparent contact angle and the instantaneous contact-line speed. Previous work (Spelt 2006) shows that such a type of relation exists for the corresponding two-dimensional problem but for a local maximum angle between the interface and the wall; and it is not known at present whether this still holds true for the three-dimensional problem, and what this relation is. On this point, the present work follows up on a previous experimental study by Le Grand, Daerr & Limat (2005) for drops sliding down an inclined plane.

A second regime is found to occur beyond a second critical value of Ca or We (higher than that for the onset of motion), wherein small drops (or, possibly, virtually the entire droplet) are entrained by the surrounding shear flow from the initial droplet. The ability to predict the onset of entrainment is of practical importance in, for instance, the development of models for the rate of entrainment and deposition in annular and stratifying annular flows of oil/water/gas mixtures (see Pan & Hanratty

2002). A practical issue here is to know under what circumstances part of the pipe is not covered by a film (e.g. the top of a large-diameter horizontal pipe in stratified flow) such that corrosion inhibitors in the liquid phase are no longer efficient, motivating investigations into the fate of deposited drops in the presence of a shear flow. A first insight into partial entrainment of drops from walls can be inferred from a study by Kang, Zhang & Chen (2005) for pressure-driven flow in a duct, to which we refer readers for elaborate time sequences of the drop shape and the flow. It remains unclear to what extent the onset of motion coincides with the onset of entrainment (the simulation method of Kang *et al.* 2005 did not allow for contact-angle hysteresis, hence their drops would always move, and only limited information was provided on the critical condition for the onset of entrainment). We therefore investigate this regime in some detail in this paper, allowing for contact-angle hysteresis and a comparison between the onset of motion and entrainment, also following earlier work by Schleizer & Bonnecaze (1999) and Spelt (2006) for the corresponding two-dimensional flow.

Furthermore, the present problem provides an excellent opportunity to investigate droplet pinch-off in the context of atomization, the advantage of the present system being that interfacial waves do not have to be tracked over a large distance. At the very final stages of the entrainment process, one would expect an approach towards a universal pinch-off regime (see Lister & Stone 1998). Consideration of the full numerical simulation data on such an approach in the dripping of drops from a faucet (Notz & Basaran 2004) suggests that this transition in the present flow is likely to be beyond the reach of the numerical discretization at our disposal, bearing in mind that the entire large-scale flow in both fluids must be simulated in a reasonable period of time. In any event, little appears to be known about the earlier stage, during which ligaments are stretched by the oncoming shear flow (before the transition towards the asymptotic regime), and numerical methods such as that used here are ideally suited to investigate this process further. In particular, we determine here whether a model proposed by Marmottant & Villermaux (2004*a*) (or an adapted version of that) can be used to track the main stage of the ligament growth process with potential use in the prediction of the volume of entrained drops. We present results for different values of the grid spacing to investigate convergence of the results.

For these purposes, we use the numerical scheme of Ding, Spelt & Shu (2007), which was further tested against simulations based on a level-set approach for spreading drops by Ding & Spelt (2007*a*,*b*). In this scheme, a diffuse-interface method is used to track the evolution of the fluid–fluid interface, which allows for a density and viscosity contrast in fluids. The stress singularity at moving contact lines is resolved by the wetting conditions at the solid wall, resulting in an effective slip length λ proportional to the thickness of the diffuse-interface (Ding & Spelt 2007*b*). The limitation of this investigation is (in addition to an attempt to resolve the final stages of a pinch-off process discussed above) that small values of the effective slip length that would be representative of experiments on, for instance, an O(mm) drop is beyond the reach of such full numerical simulations. Nevertheless, the present numerical method and related methods have been successfully applied in previous work to identify various trends involving moving contact lines (Spelt 2006; Ding & Spelt 2007*a*, 2008). It is possible to vary the effective slip length in the present simulations to some extent, and we show in § 3.6 that the slip length could be reduced sufficiently here to change a quasi-steady state regime wherein a drop moves eventually at a constant speed into an entrainment event.

In summary, after presenting the numerical method in § 2, the quasi-steady regime is investigated (§ 3.1), followed by the onset of entrainment of a pinned drop (§ 3.2)

Parameter	Definition
θ_A	Advancing contact angle
θ_R	Receding contact angle
θ_0	Initial contact angle
θ_m	Local maximum angle between the interface and the wall
R	Length scale; $R \equiv (1.5V/\pi)^{1/3}$ for a drop with a volume of V
λ	Effective slip length
Re	Reynolds number; $Re = \rho\dot{\gamma}R^2/\mu$
Ca	Capillary number; $Ca = \mu\dot{\gamma}R/\sigma$
C_n	Cahn number; $C_n = \epsilon/R$
Pe	Péclet number; $Pe = \dot{\gamma}R^2/(M_c\Psi_c)$
Ca_c	Critical capillary number for onset of entrainment
Ca_{cl}	Dimensionless instantaneous contact-line speed
$Ca_{cl,s}$	Dimensionless contact-line speed at quasi-steady state
$X_T(t)$	x position of the downstream tip of the ligament at the time t
r_{min}	Radius of pinching neck of a ligament
t_R	Time ligament rupture; $t_R \equiv t_0 - t$ where t_0 is the time of rupture

TABLE 1. Relevant parameters in problem description and results. Additional parameters are indicated in figure 1.

and the approach to pinch-off (§§ 3.3–3.5). Entrainment and detachment of a moving drop is investigated in § 3.6.

2. Problem statement and methodology

2.1. *Problem statement*

A sketch of the problem studied here is provided in figure 1 and the relevant parameters are defined in Table 1. The two fluids involved are assumed to be immiscible, incompressible and viscous, and to have a constant (non-zero) coefficient of surface tension σ. The viscosity and density of the surrounding fluid is μ and ρ, respectively, and the ratio of viscosity (density) of the droplet to the surrounding fluid is denoted by λ_μ (λ_ρ). The shear rate $\dot{\gamma} = U/H_T$ is maintained by moving the upper boundary of the domain, located at $z = H_T$, at a constant speed U. The equations of motion are made dimensionless using $1/\dot{\gamma}$ and a specific droplet radius $R = (1.5V/\pi)^{1/3}$ as the characteristic time and length scale, respectively, where V is the drop volume. The resultant dimensionless numbers are $Re(=\rho\dot{\gamma}R^2/\mu)$ and $Ca(=\mu\dot{\gamma}R/\sigma)$. Effects of gravity are ignored here in order to limit the number of dimensionless parameters; hence, a Bond number $\rho(\lambda_\rho - 1)gR^2/\sigma$ is assumed to be small. The effect of gravity studied for the onset of droplet motion in shear flow has been investigated for the creeping-flow regime by Dimitrakopoulos (2007b). Two representative contact-angle hysteresis windows are considered: $\theta_A = 90°$, $\theta_R = 40°$ and $\theta_A = 90°$, $\theta_R = 70°$. The initial shape of the droplet is taken to be a spherical cap, with a uniform contact angle θ_0 ($\theta_R \leqslant \theta_0 \leqslant \theta_A$). Five cases will subsequently be referred to are: Case A ($\theta_A = 90°$, $\theta_R = 40°$ and $\theta_0 = 90°$); Case B ($\theta_A = 90°$, $\theta_R = 40°$ and $\theta_0 = 40°$); Case C ($\theta_A = 180°$, $\theta_R = 0°$ and $\theta_0 = 90°$); Case D ($\theta_A = 90°$, $\theta_R = 70°$ and $\theta_0 = 90°$); and Case E ($\theta_A = 90°$, $\theta_R = 70°$ and $\theta_0 = 70°$), among which Case C corresponds to a pinned droplet. In all calculations reported here, the symmetry of the problem in the (x,y) plane is exploited by simulating half of the droplet. Simulations are normally carried out in a domain of $16.8 \times 2 \times 2$ on a mesh of $500 \times 60 \times 60$, and a longer domain may be used

depending on the case investigated. Initially, the droplet rests on the solid substrate at $x = 3$, and is then suddenly subjected to the surrounding simple shear flow. The boundary conditions are imposed as follows. At the inlet, $\partial u_x/\partial x = 0$ and $u_y = u_z = 0$; at the outlet boundary, $\partial \boldsymbol{u}/\partial x = 0$, where (u_x, u_y, u_z) are the velocity components in the (x, y, z) directions (see figure 1). At the symmetric cross-section, i.e. the (x,z) plane at $y = 0$, symmetry boundary conditions are used (with $u_y = 0$), while at the other side of boundary (normal to the y direction) $\partial \boldsymbol{u}/\partial y = 0$. No-slip boundary conditions are enforced at the upper and lower boundaries. The initial velocity field outside the droplet corresponds to the imposed shear flow, whereas inside the droplet it is set to zero. We have conducted numerical experiments for the entrainment of a pinned droplet at $Re = 18$ with zero initial velocity everywhere except at the impulsively moving upper wall. Those computations show that the droplet takes an excessive time for the occurrence of entrainment, whereas this change in the initial condition for the velocity field does not affect the critical value for the onset of entrainment.

2.2. *Diffuse-interface method and wetting conditions*

We use a diffuse-interface model for incompressible immiscible fluid flows with large density and viscosity ratios (Ding *et al.* 2007), with appropriate wetting conditions at the solid boundary, which allows for a moving contact line (Jacqmin 2000; Ding *et al.* 2007). The numerical method used here is essentially the same as that used in our previous work on the onset of motion of drops on a wall (Ding & Spelt 2008). In this method, a sharp interface between two fluids is replaced by an interfacial region of finite thickness. The volume fraction of one of the fluids, denoted by C, is used to describe the position of the interface (with $0 \leqslant C \leqslant 1$). The thickness of the diffuse interface is artificially determined by an interface parameter ϵ and $\epsilon \ll R$ is required for accurate simulations. Taking both accuracy and efficiency into account, we choose here $\epsilon = 0.5\Delta x$, resulting in a Cahn number $C_n = \epsilon/R = 0.0167$, where Δx is the mesh spacing. As a result, local density and viscosity, as well as the pressure field, vary relatively smoothly across the interface. The governing equation for C is the dimensionless Cahn–Hilliard equation

$$\frac{\partial C}{\partial t} + \nabla\cdot(\boldsymbol{u}C) = (1/Pe)\nabla^2\Psi, \tag{2.1}$$

where Ψ $(= C_n^{-1}\phi'(C) - C_n\nabla^2 C)$ is the chemical potential, $\phi = C^2(1-C)^2/4$ is the bulk energy density, $Pe = \dot{\gamma}R^2/(M_c\Psi_c)$ is the Péclet number, M_c and Ψ_c are the characteristic values of mobility and chemical potential. In this study, we choose $Pe = C_n^{-2}$ in all simulations. As in the previous work, the position of the interface is henceforth defined by the contour $C = 0.5$. The velocity $\boldsymbol{u}$ is divergence-free, and is obtained from solving the Navier–Stokes equations using a projection method (see Ding *et al.* 2007, where extensive test results can be found). Following earlier work by Jacqmin (2000), we investigated the effective slip length resulting from the presence of the finite interfacial layer by comparing results for axisymmetric droplet spreading with those obtained from a level-set method wherein a slip-length formulation was used (Ding & Spelt 2007*a*). The effective slip length λ (when using a no-slip condition for the velocity field) is approximately twice the measure of the thickness of the diffuse-interface, i.e. $\lambda = 2\epsilon$. Contact-angle hysteresis is represented as described by Ding & Spelt (2008), i.e. through prescription of an appropriate boundary condition for C at the solid substrate (Ding & Spelt 2008). Essentially, at each time step, the local value of the contact angle is determined. If this value is outside the hysteresis window, either the advancing or the receding contact angle value is prescribed by setting the appropriate

value of C at a layer of ghost cells below the solid wall; otherwise, the C values at the corresponding ghost cells remain unchanged. This procedure extends the geometric formulation that was proposed by Ding & Spelt (2007*b*) for cases without hysteresis, at the part of contact line where either θ_A or θ_R needs to be enforced, i.e.

$$\boldsymbol{n}\cdot\nabla C = -\tan(\pi/2-\theta)|\nabla C - (\boldsymbol{n}\cdot\nabla C)\boldsymbol{n}|, \tag{2.2}$$

where $\theta=\theta_A$ or $\theta=\theta_R$ depending on the instantaneous local contact angle. To ensure that there is no penetration of diffusive fluxes, $\boldsymbol{n}\cdot\nabla\Psi=0$ is explicitly enforced at the solid wall. In addition to wetting conditions implemented at the lower solid wall, other boundary conditions for C are: $C=0$ at $x=0$, $y=2$ and $z=2$; $\partial C/\partial x=0$ at $x=16.8$ and $y=0$. Details of general numerical tests with this code (including convergence studies) can be found in Ding *et al.* (2007). Although mass conservation (in the sense of a volume integral of C over the entire domain) with this method is of machine accuracy, in the presence of contact lines, we try to avoid small overshoots and undershoots arising from the implementation of the wetting conditions by strictly restricting the upper and lower bounds of C values, such that $C=1$ if $C>1$ and $C=0$ if $C<0$, which is found to slightly affect volume conservation. Tests show that for instance in the rather complex flow shown in figure 14, the error in the total volume of the droplet phase does not exceed 2.7 %. A detailed comparison for the present problem setup with results obtained by Dimitrakopoulos & Higdon (1998) (who used a boundary-element approach) can be found in Ding & Spelt (2008). Finally, at appropriate points below, we include results obtained for different grids.

3. Results

In this study, we mainly restrict our attention to the cases wherein the density and viscosity of the droplet have the same values as the surrounding fluid, i.e. $\lambda_\mu=\lambda_\rho=1$. The effects of viscosity and density contrast are considered at some points in §§ 3.4–3.5. The effectively slip length in the simulations has a value of $0.03R$ unless stated otherwise.

3.1. *Sliding droplets*

A typical three-dimensional view of a droplet sliding at almost constant velocity and shape is shown in figure 1 for $Re=18$ and $Ca=0.17$. Figure 2(*a*) is a visualization of the corresponding contact line and the velocity vectors in the (x, y) plane close to the solid wall ($z=0.0167$). The shape of the contact line is seen to be similar to that assumed in the analysis by Dussan V. (1987): two curved ends connected by parallel sides. At the parallel sides the local velocity is tangential to the contact line (we have checked that at the parallel sides the local contact angle value changes from θ_R to θ_A). At the curved downstream (and to some degree the upstream) end, the velocity is approximately normal to the contact line and approximately equal to the speed of the droplet times the cosine between the x axis and the vector normal to the contact line. (We note here that there is a small effect of the small height $\Delta z/2$ whereat the vectors have been plotted at the upstream side, due to the relatively small value of the contact angle there.) This has also been found experimentally by Rio *et al.* (2005) for droplets sliding down at an inclined wall. The inference drawn by those authors from this, that the contact angle therefore only depends on the local value of the capillary number based on the contact-line speed, is investigated below.

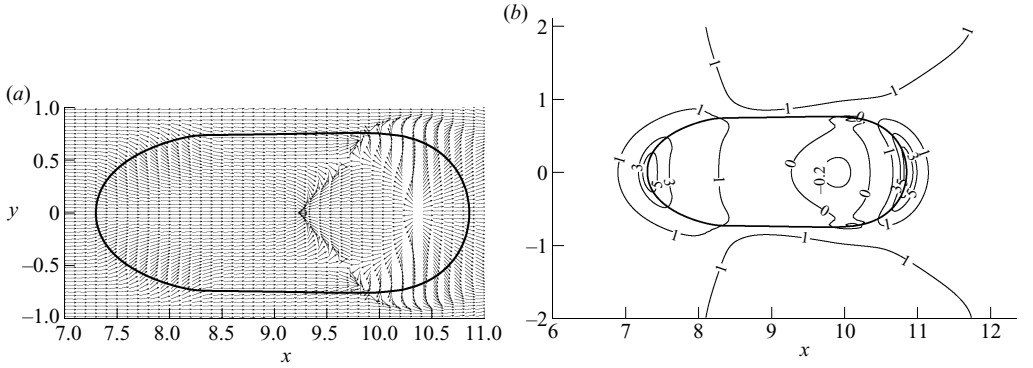

FIGURE 2. Velocity vectors and shear strain near the solid wall at $Re = 18$ and $Ca = 0.17$ for Case *A*. The corresponding three-dimensional view is shown in figure 1. (*a*) Contact line and velocity vectors at $z = 0.0167$. The vectors are all of equal length and indicate the direction of the velocity only. (*b*) The distribution of shear strain (i.e. $\partial u_x/\partial z$). The shear strain has been non-dimensionalized by the shear flow rate $\dot{\gamma}$.

The initial shape of a droplet is known to potentially have a significant effect on the critical conditions for the onset of motion, i.e. the droplet would move continuously beyond the criticality (see Dimitrakopoulos & Higdon 1998), as well as its temporary contact-line motion at the early stage (see Ding & Spelt 2008). It is therefore of interest to investigate whether and how the initial shape affects sliding droplets. For this purpose, numerical simulations have been carried out for droplets of equal volume but with different initial configurations (Cases *A* and *B*, *D* and *E* in the problem definition section). A comparison is made in figure 3, where snapshots of moving droplets for Cases *A* and *B* are shown as a function of time at $Re = 18$ and $Ca = 0.252$. It is seen that the difference in the initial shape causes different droplet motion at an early stage. For example, it is the upstream part of the contact line in Case *A* that starts to move first, whereas it is the downstream part of the contact line in Case *B*. However, once the droplets have completely departed from their initial position, they evolve into a similar elongated shape shortly. A comparison of the droplet shape between Cases *A* and *B* at this stage is shown in figure 4 (here, the drops have been shifted such that their downstream ends coincide, to facilitate the comparison). We can see that the contact lines and cross-sections of the two droplets virtually overlap, even though at this point the droplets have not quite reached a quasi-steady state, which in this case would require an excessive computational effort to approach; results of the approach to steady state are discussed below. This shows that the initial shape of a droplet may have little effect on the quasi-steady state of a steadily moving droplet, unlike the onset of motion. This has been verified by further tests on Cases *A* and *B* and *D* and *E* at representative Reynolds and capillary numbers. Figure 5 gives a quantitative presentation of geometrical change of the droplet as a function of time, in terms of length, width and height. In all three cases (Cases *A* and *B* at $Re = 3$ and $Ca = 0.3$, Cases *D* and *E* at $Re = 3$ and $Ca = 0.3$ and Cases *D* and *E* at $Re = 18$ and $Ca = 0.2$), the geometrical parameters appear to converge, although the convergence of the length is much slower than that of the width and the height.

In previous work, a force balance of droplets has been shown to be successful in explaining the critical value of *We* for the onset of motion (see Ding & Spelt 2008), and we revisit this balance here to see whether this can be used to develop a

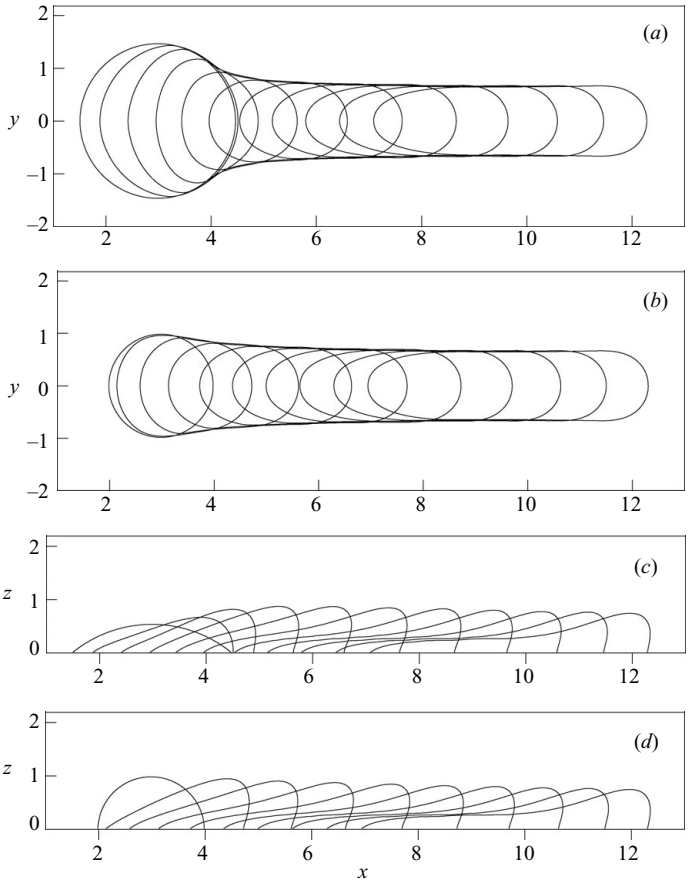

FIGURE 3. Snapshots of the droplet at successive times of a regular interval at $Re = 18$ and $Ca = 0.252$ for Cases A and B. Contact lines are shown in (a) and (b), while cross-sections are shown in (c) and (d). In (a) and (c) the initial contact angle is $\theta_0 = 40^\circ$ and in (b) and (d) it is $\theta_0 = 90^\circ$.

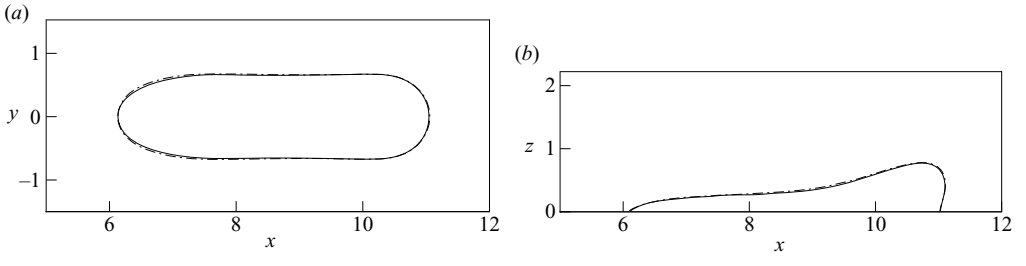

FIGURE 4. Comparison of droplet shape between $\theta_0 = 40^\circ$ (solid line) and 90° (dash-dotted line) at $Re = 18$ and $Ca = 0.252$. (a) Contact line and (b) cross-section.

prediction of the drop speed at a quasi-steady state (denoted henceforth by V_s). At the quasi-steady state, there is a balance between the force exerted by the surrounding fluid on the moving drop, the wall stress exerted on the drop and an adhesive force arising due to the intersection of the fluid/fluid interface by the wall. Hence we must

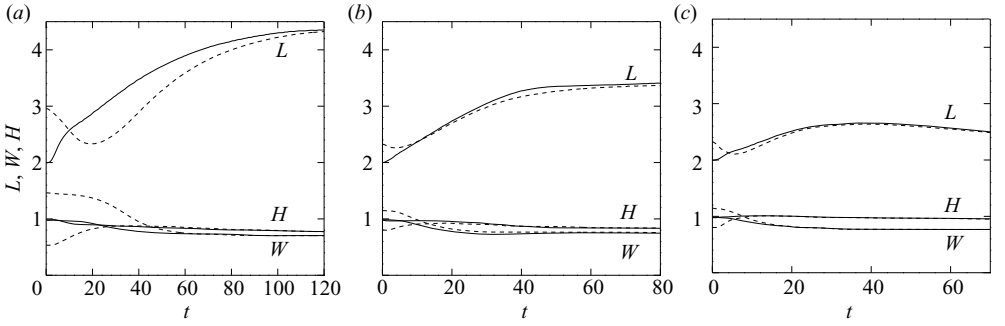

FIGURE 5. Time evolution of moving drops on a solid substrate in terms of length (L), width (W) and height (H). Initial configurations are: $\theta_0 = \theta_A$ (solid line) and θ_R (dashed line). (a) Cases A and B at $Re = 3$ and $Ca = 0.3$; (b) Cases D and E at $Re = 3$ and $Ca = 0.3$; (c) Cases D and E at $Re = 18$ and $Ca = 0.2$.

have, in dimensional form,

$$\int_{S_I} \boldsymbol{n} \cdot \boldsymbol{T}\,\mathrm{d}S + \int_{S_W} \boldsymbol{n}_W \cdot \boldsymbol{T}\,\mathrm{d}S + \sigma \oint_{CL} \boldsymbol{t}\,\mathrm{d}l = 0, \tag{3.1}$$

where S_I is the fluid/fluid interface, S_W is the area of the wall wetted by the drop, CL is the contact line; $\boldsymbol{n}$ and $\boldsymbol{n}_W$ are the unit vectors (pointing away from the drop) normal to the drop surface and the wall, respectively; $\boldsymbol{T}$ is the stress tensor; and the vector $\boldsymbol{t}$ is a unit vector tangent to the interface, in the plane spanned by the vectors normal to the wall and the contact line, and is pointing into the wall. At quasi-steady state only the x-component of this balance needs to be considered, and we briefly discuss scaling of this component of the three terms in (3.1). Following the arguments by Ding & Spelt (2008), we tentatively write the force exerted by the surrounding fluid on the drop as $\alpha_v \mu \dot{\gamma} R^2 + \alpha_i \rho R^2 (\dot{\gamma} R - V_s)^2$, where $\alpha_{v,i}$ are unknown factors that will depend on the geometry of the drop and, in principle, all dimensionless parameters in the problem (this force has been determined analytically for a hemispherical droplet in Stokes flow by Sugiyama & Sbragaglia 2008). The wall stress can partially be absorbed into this expression. However, there is a large additional contribution to the wall stress arising from the motion of the contact line; this can be seen in figure 2(b), consistent with Kang *et al.* (2005). We tentatively write this additional contribution as $\alpha_m \mu V_s R$, where α_m is assumed to depend on the dimensionless effective slip length λ/R. The final contribution in (3.1) arises from the intersection of the drop surface with the wall, and can be written as $\sigma \oint_{CL} \boldsymbol{e}_x \cdot \boldsymbol{n}_c \cos\theta\,\mathrm{d}l$, where $\boldsymbol{e}_x$ and $\boldsymbol{n}_c$ are the unit vectors in the x-direction and normal to the contact line in the (x, y) plane, respectively. If the contact angle θ has a unique value along the contact line, the integration can be simplified and yields $\sigma \cos\theta \oint_{CL} \mathrm{d}y$. It is clear that it gives a zero value for a closed contact line no matter if the contact line has fore/aft symmetry. For a sliding drop with contact-angle hysteresis, the contact line has two curved ends at which the contact angles are θ_R at the upstream and θ_A at the downstream, and parallel sides along which contact angles change from θ_R to θ_A. In this case, the integration yields $\sigma l_w (\cos\theta_R - \cos\theta_A)$, where l_w is the arclength of the contact line. We write this as $\alpha_s \sigma R(\cos\theta_R - \cos\theta_A)$, where $\alpha_s = l_w/R$. Hence, a force balance over the droplet yields

$$\alpha_m Ca_{cl,s} = \alpha_v Ca + \alpha_i We(1 - Ca_{cl,s}/Ca)^2 - \alpha_s(\cos\theta_R - \cos\theta_A), \tag{3.2}$$

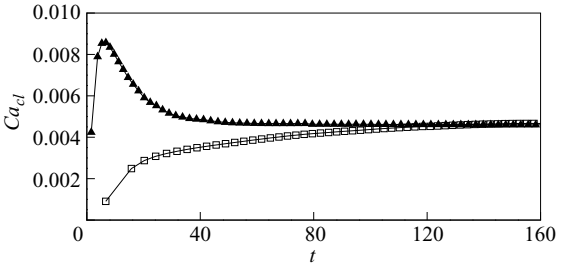

FIGURE 6. Contact-line speed as a function of time at $Re = 1.08$ and $Ca = 0.21$ for Case A. Filled triangles denote the downstream-end contact-line speed, while open squares denote the upstream-end contact-line speed.

where $Ca_{cl,s} = \mu V_s/\sigma$. Only a positive resulting value for $Ca_{cl,s}$ is admissible; a negative result means the droplet will eventually grind to a halt (the contact angle at the curved ends will then be inside the hysteresis window and the last term in (3.2) must be modified accordingly). Naturally, hysteresis results in the critical condition for the onset of motion (obtained by setting $Ca_{cl,s} = 0$) of Ding & Spelt (2008).

For systems without hysteresis and inertial effects, we find $Ca_{cl,s} = \alpha_v Ca/\alpha_m$. We should expect α_m to increase when the effective slip length is reduced, naturally leading to a reduction in the drop speed. In that case, the drop speed is the result of the balance between viscous drag exerted on the drop and the wall stress resulting from contact-line motion. The results by Kang *et al.* (2005) for a droplet with zero contact-angle hysteresis do show this linear regime. This linear regime has also been observed in our simulations for sliding droplets with a moderate window of hysteresis, at low Reynolds numbers in particular. Figure 6 presents a typical example of a moving droplet approaching the quasi-steady state, at $Re = 1.08$ and $Ca = 0.21$. The instantaneous dimensionless contact-line speed $Ca_{cl} = \mu U_{cl}/\sigma = CaU_{cl}/(\dot{\gamma} R)$, where the contact-line speed U_{cl} was obtained by determining the contact-line position from C using linear interpolation, and subsequently differentiating the position numerically with time. To avoid oscillations arising from the linear interpolation in the determination of the contact-line position, U_{cl} is only computed when the contact line has moved at least a distance of Δx since the last U_{cl} computation. It can be seen in figure 6 that the contact-line speeds at the upstream and downstream end converge asymptotically to a constant value with time.

Figure 7(a) shows the contact-line speed at the quasi-steady state (i.e. $Ca_{cl,s}$) as a function of Ca, approximately under creeping flow conditions for Case A ($Re = 1.08$). Compared with the results for a case without hysteresis, $Ca_{cl,s}$ does not start to increase from zero when we increase the value of Ca from one just below criticality of the onset of motion to one just above criticality of the onset of motion. It was shown by Ding & Spelt (2008) that $Ca = 0.126$ is just below the critical value for the onset of motion at $Re = 1.08$, whereas figure 7(a) suggests the droplet would approximately have a speed of $Ca_{cl,s} = 0.006$ if it had been in motion. This jump in contact-line speed may be due to changes in the shape of the contact line when comparing between sliding and stationary droplets, especially regarding the arclength of the contact line. We can see from figure 7(b) that at $Ca = 0.126$, i.e. just below the critical value of onset of motion, the stationary droplet has two small lateral 'wings', which are not seen for sliding droplets. These wings correspond to the part of the contact line that the contact angle changes from θ_R to θ_A, whereas only parallel straight sides are allowed for steadily moving contact lines (Dussan V. & Chow 1983). Moreover, they

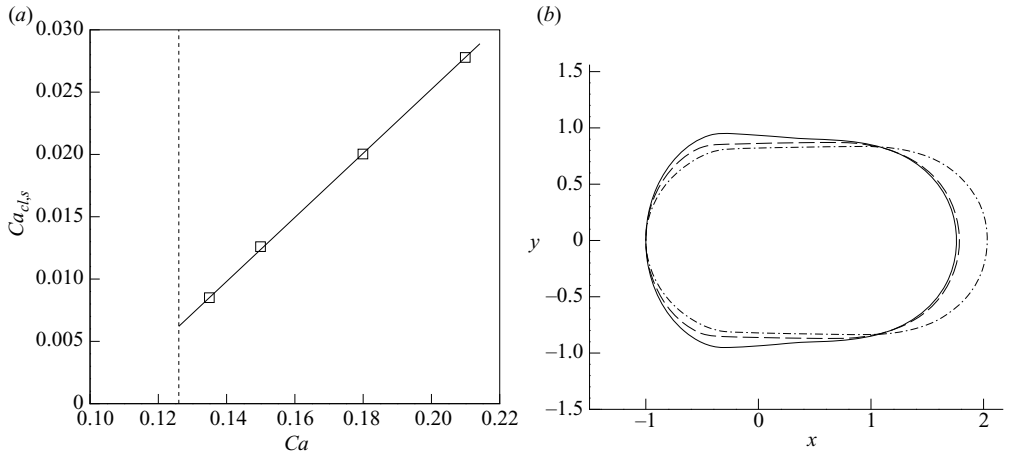

FIGURE 7. Sliding drops in a quasi-steady state at $Re = 1.08$ for Case A. (a) Dimensionless contact-line speed as a function of Ca; (b) contact-line shapes, where the solid line represents the results just below criticality for the onset of motion (i.e. $Ca = 0.126$ which is equivalent to $Ca = 0.1$ in Ding & Spelt 2008), the dashed line represents the results at $Ca = 0.15$ and dash-dotted line represents the results at $Ca = 0.21$.

may provide a small additional resistive force. It is reasonable to expect that this jump in contact-line speed is more significant for Case B, because Case B requires a larger value of Ca to achieve an onset of motion than Case A (see Dimitrakopoulos & Higdon 1998 and Ding & Spelt 2008). In conclusion, the speed of steadily moving droplets is still linear in Ca in the presence of contact-angle hysteresis, if the shear rate is beyond the critical value for the onset of motion. Furthermore, we find that the shape of droplets at quasi-steady state is rather different for, for instance, different values of Ca, which would modify the unknown coefficients in (3.2).

For the corresponding two-dimensional problem, the contact-line speed has been found in previous work (Spelt 2006) to be associated directly with the local maximum angle that the interface makes with the wall, θ_m, and results for different values of Ca and λ/R could be collapsed onto a single curve. For droplet spreading without the external forcing of a shear flow, this maximum angle may be interpreted as an apparent contact angle (see Ding & Spelt 2007*a*, and references therein). The present numerical code has been used in our previous work to investigate inertial effects in the relation between the maximum angle and the contact-line speed in droplet spreading (Ding & Spelt 2007*a*). In this system, the contact-line motion is not solely due to conventional spreading, but due to the imposed shear flow. Hence, Spelt (2006) found the results for θ_m to deviate from a Cox–Voinov relation; also, the maximum angle was observed not to occur in the immediate vicinity of the contact line. Nevertheless, the results for θ_m for different values of Ca and slip length collapsed onto a single curve.

With these considerations in mind, we investigate here the conditions near the downstream and upstream ends of the contact line for an almost-steadily moving drop in three-dimensions (the study by Spelt 2006 being for two-dimensional drops). Figure 8 shows the angle between the tangent of the interface and the horizontal, as a function of the distance to the downstream and upstream ends of the contact line. At the downstream side of the drop, it can be seen that the angle initially increases with the distance from the contact line and gradually reaches a maximum value θ_m

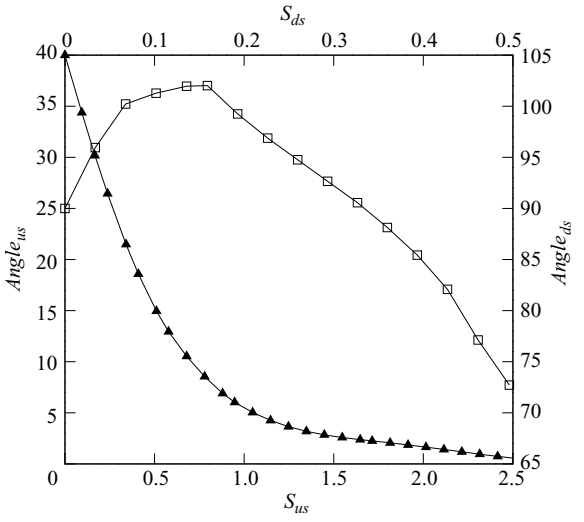

FIGURE 8. Angle of the tangent to the interface intersecting the horizontal (measured in the vertical plane containing the drop centreline) as a function of the distance to the contact line, for Case *A*, $Re = 18$ and $Ca = 0.252$. The results for the interface at the downstream (open □) are presented by the right and upper coordinates and denoted by the subscript *ds*, whereas the results for the interface at the upstream (filled Δ) are presented by the left and bottom coordinates with the subscript *us*. Note that the angle distribution shown here corresponds to the last snapshot in figure 3(*d*).

($= 102^\circ$ at $s = 0.17$). The results near the upstream side of the contact line are similar to those reported by Spelt (2006), in the sense that the angle decreases with the distance and approaches zero away from the contact line for an elongated drop, and that a maximum value in the slope occurs rather far away from the contact line on the downstream side of the drop.

Figure 9 shows θ_m as a function of the local contact-line speed for various values of Ca. In principle, a very fine grid would be needed to resolve the highly curved interface in the vicinity of the contact line and the resultant small-scale fluid flow. However, the present results for sliding droplets suggest that the relation between this angle and the instantaneous velocity is universal, with qualifications. We can see that for $Ca = 0.17$ and 0.30 the results are more or less on the same curve (as are those that were obtained with a different grid when keeping the same interfacial thickness), where θ_m increases with the instantaneous contact-line speed when the droplet starts to move and then is accelerated. When the contact-line speed reaches its peak value, it slows down and appears to approach a constant value (a quasi-steady state). During the deceleration in the contact-line speed, we find that θ_m decreases following the same curve. At $Ca = 0.32$, drop entrainment occurs at the top of the droplet (drop entrainment is investigated in detail in subsequent sections), and θ_m reaches 180 degrees at the same time. After pinch-off of a small droplet the part of the original drop remaining on the solid wall still moves but θ_m has dropped sharply. Remarkably, the relation between θ_m and contact-line speed follows the same curve as before breakup.

The results are compared in figure 9 with the corresponding results for the two-dimensional problem for different values of Ca and the slip length at a single

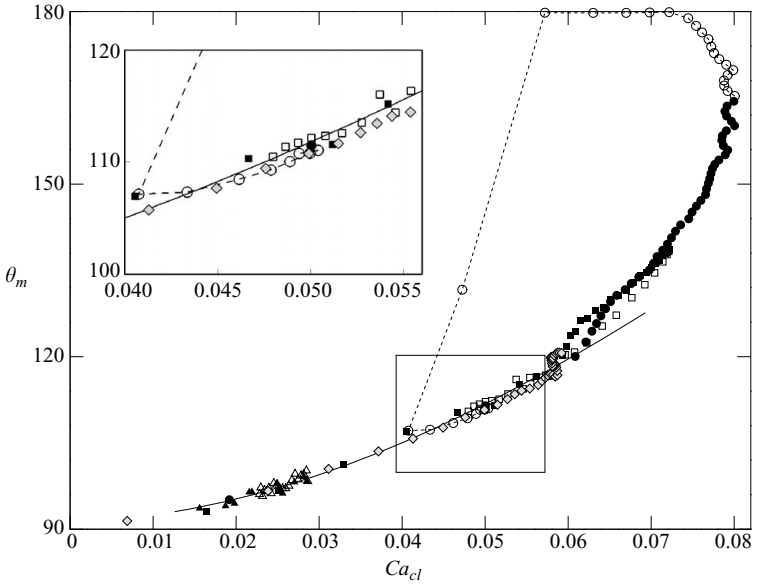

FIGURE 9. θ_m as a function of dimensionless instantaneous contact-line speed Ca_{cl} for Case *A* at $Re = 18$, where $Ca_{cl} = \mu U_A/\sigma = CaU_A/(\dot{\gamma}R)$ and U_A is the instantaneous contact-line speed at the downstream end of the contact line. Results are shown for $Ca = 0.17$ (Δ), 0.30 ($\square$) and 0.32 (O). Filled and open symbols correspond to results prior and after the contact-line speed reaches a maximum value, respectively. The dashed line is drawn to guide the eye. Droplet entrainment occurs at $Ca = 0.32$. The solid line corresponds to (3.3) with $\lambda/R = 0.018$. Results on a half mesh size but with the same thickness of the diffuse-interface (or the same effective slip length) are shown for $Ca = 0.30$ (grey filled $\diamond$).

intermediate value of Re, which could conveniently be fitted to (Spelt 2006)

$$\left(\theta_m^3 - \theta_A^3\right)^{1/3} \approx (0.12 + 5.2Ca_{cl})\ln(R/\lambda) \quad (0.01 \leqslant Ca_{cl} \leqslant 0.1) \tag{3.3}$$

(the effect of changing the Reynolds number is discussed in the next paragraph). A deviation was observed by Spelt (2006) from (3.3) when droplet entrainment was approached (we take this opportunity to correct (4.2) of Spelt 2006 accordingly; the labels in figure 15 in that paper are correct). There is no physical basis for (3.3), it merely serves as a curve fit to the data, including those for different values of the slip length; other versions wherein for instance $\theta_m = \theta_A$ as $Ca_{cl} = -0.029$ are equally possible. We conclude from figure 9 that the three-dimensional and two-dimensional results correspond quite closely when setting $\lambda/R = 0.018$ in (3.3) for the present results. The dimensionless effective slip length in the present simulations is approximately $\lambda/R \approx 0.03$ (based on Ding & Spelt 2007*a*). Since the definition of macroscopic length scale R for the three-dimensional system is different from that for the two-dimensional system, a mere $O(1)$ difference between the values of λ/R seems reasonable.

These findings are robust at relatively large values of Re. Upon increasing Re, θ_m is seen in figure 10, after first reaching very large values during an initial transient, to approach the same curve as that for moderate Re, and the results are again close to (3.3). But there is a substantial effect of the value of Re on these results when approaching small Re. At small Re, the value of Ca_{cl} is seen in figure 10 to be much larger whereas θ_m is still fairly small, i.e. there is a substantial departure from (3.3).

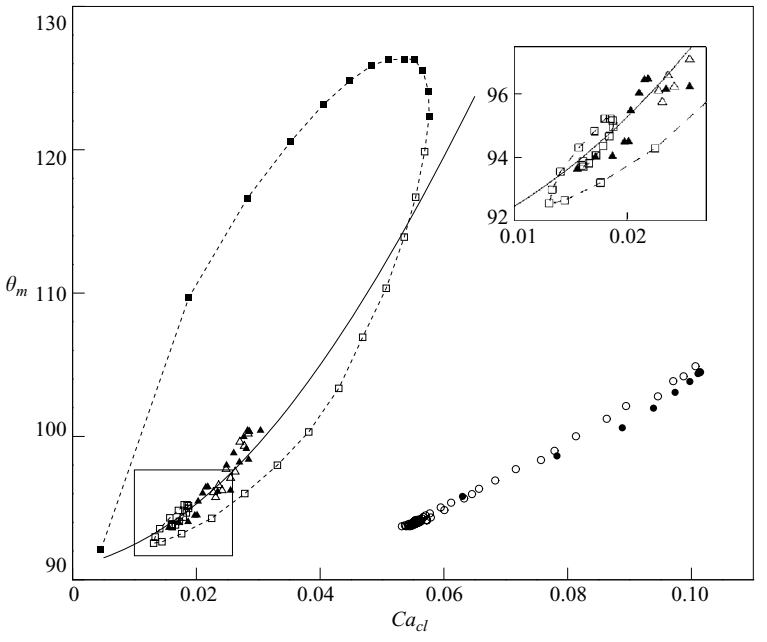

FIGURE 10. θ_m as a function of dimensionless instantaneous contact-line speed for Case A at $Ca = 0.17$. Results are shown for $Re = 1.8$ (O), 18 (Δ) and 180 ($\square$). Filled and open symbols correspond to results prior and after the contact-line speed reaches a maximum value, respectively. The solid line corresponds to (3.3) with $\lambda/R = 0.018$.

Previous work on inertial effects in droplet spreading has shown such data only to collapse at small values of Ca_{cl} (Ding & Spelt 2007*a*), suggesting that the effective slip length would have to be reduced significantly for such a collapse of the data for $Re = 1.8$ on those for larger values of Re.

3.2. *Onset of entrainment for a pinned droplet*

We start the study of the onset of entrainment with that for a droplet pinned on a wall, Case C; the effect of sliding on entrainment is studied in a subsequent section. Snapshots of the cross-section in the x–z symmetry plane for droplets at a value of Ca just below and just above the critical condition for the onset of entrainment are shown in figure 11 at $Re = 1.8$ and 180. At moderate Re, for the droplet at a value of Ca just below criticality, the drop is initially very strongly deformed before reaching its steady state, as shown by the successive snapshots in figure 11(c). At later times, the elongation continues and gradually rotates towards the flow direction until surface tension becomes larger than viscous forces and pulls back the ligament. The droplet ends up with a 'thumb'-like shape. When Ca is slightly larger than the critical value, the resultant slender ligament becomes unstable and breaks up in a very short time, when the radius of the 'neck' of the ligament becomes sufficiently small for capillary forces to become significant. From figure 11(c) we conclude that the curvature in the ligament neck was insufficient for this to happen in that case. Compared with the corresponding two-dimensional problem (Spelt 2006), we find that three-dimensional results for the onset of entrainment are significantly different. Below criticality, in two-dimensional simulations, droplets are seen to be hardly deformed at moderate Re compared with that at low Re, whereas the present three-dimensional results signify the opposite. Also, in our three-dimensional numerical studies the size of the

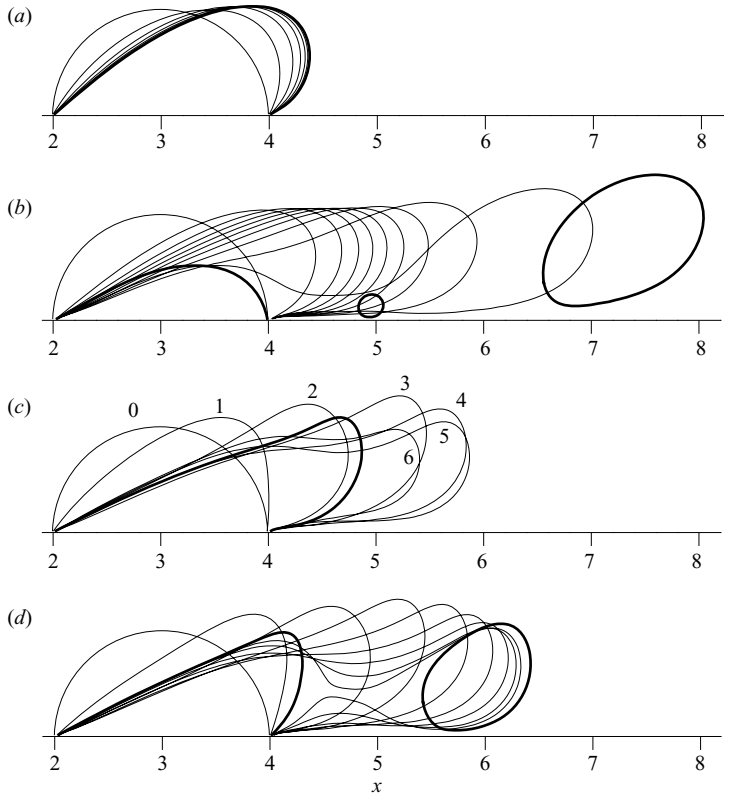

FIGURE 11. Successive snapshots for a pinned droplet (i.e. Case *C*) for Ca just below and above the critical value of onset of entrainment at low and moderate Re. (*a*) $Ca = 0.136$ and (*b*) $Ca = 0.15$ at $Re = 1.8$; (*c*) $Ca = 0.115$ and (*d*) $Ca = 0.120$ at $Re = 180$. The thick curves represent the droplet shapes at the steady state in (*a*) and (*c*), whereas the snapshot after pinch-off in (*b*) and (*d*). The numbers in (*c*) indicate the time sequence of the snapshots.

entrained drop is seen to decrease when Re is increased and Ca is just above the criticality of onset of entrainment.

Figure 12 shows the critical condition for the onset of entrainment of a pinned droplet, in terms of the critical capillary number, Ca_c, as a function of Re. We can see that Ca_c decreases only by a modest amount as Re is increased (considering the substantial range of Re studied) and appears to approach a constant value at moderate Re, before dropping off at larger Re. This is in sharp contrast to the results from previous work (Spelt 2006) (as are the shapes at criticality, as discussed above), where in a smaller range of values of Re, the critical Weber number $We_c = ReCa_c$ clearly approached a constant value at moderate values of Re. These results therefore suggest that entrainment is generally determined by the combined effects of surface tension and viscous forces. Although a significant inertial effect is seen in the droplet deformation just below Ca_c at moderate Re, and the volume of entrained drops beyond Ca_c as discussed above, but this does not appear to have a strong effect on Ca_c at low and moderate values of Re.

Although the results discussed above are for a pinned contact line, they are relevant for smaller windows of contact-angle hysteresis also. During the entire duration of all simulations reported in this section, the contact angle values at the contact line (not θ_m)

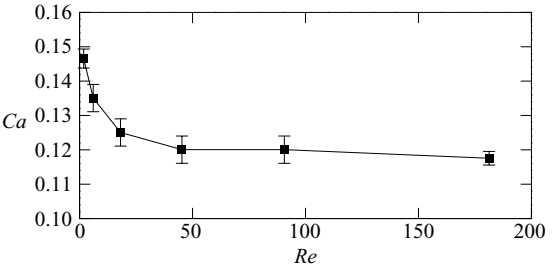

FIGURE 12. Critical capillary number of the onset of entrainment as a function of Reynolds number for a pinned droplet (i.e. Case C; $\lambda_\mu = 1$, $\lambda_\rho = 1$). The upper bound of the error bar represents the lowest Ca at which the entrainment occurs in the simulation, whereas the lower bound represents the highest Ca at which no entrainment is observed (the solid squares represent the average of these two bounds). A test case at $Re = 181$ showed no effect of changing the grid spacing by a factor of 2 when keeping the CFL number constant.

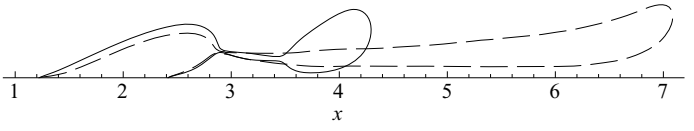

FIGURE 13. Snapshots of pinned droplets at time of breakup for $Re = 71.6$, $\lambda_\rho = 1$, $\lambda_\mu = 1$, $Ca = 0.126$ (solid line) and $Ca = 0.252$ (dashed line).

were found to be between 29° and 155°. This indicates that a window of 180° of hysteresis is not necessary to achieve a pinned droplet.

Although a full parametric study is not attempted here, we can report that tests have shown that the value of λ_μ may have a significant effect on the critical value Ca_c. At $Re = 71.6$, $Ca_c = 0.076$ for $\lambda_\mu = 5$, which compares with $Ca_c = 0.12$ at $\lambda_\mu = 1$. A decrease in Ca_c for onset of motion when increasing λ_μ was also observed in the creeping-flow regime by Dimitrakopoulos & Higdon (1998); the creeping-flow analysis by Sugiyama & Sbragaglia (2008) shows that the dimensionless force exerted on the drop increases with increasing λ_μ. This is in sharp contrast with the critical value of a capillary number for the breakup of a freely suspended drop by shear, which is known to increase strongly with λ_μ for creeping flows and insensitive to λ_μ at relatively large Re (e.g. Khismatullin *et al.* 2003). This difference is likely to be affected by the restrictions posed by the adjacent wall on the rotational motion of the drop (a circulating flow is set up inside the drop that plays an important role for freely suspended drops) and suggests a comparison with results for a drop in an extensional flow instead. The reduction in Ca_c upon an increase in λ_μ from unity to 5 is indeed consistent with previous results for that case (Rallison 1984).

3.3. *Qualitative behaviour during entrainment events*

In figure 13 the cross-sections of droplets at the time of breakup are shown for a value of Ca close and well above the critical value for entrainment, at the same value of Re. For $Ca = 0.126$ the ligament breaks up while still being very short and two pinching necks are observed. At $Ca = 0.252$ (also at $Ca = 0.19$, not shown) a longer ligament is observed and the necking and rupture takes place next to the mother droplet. At $Ca = 0.38$ an onset of capillary instability is observed (not shown). We have also tested the sensitivity of the behaviour shown in figure 13 to the viscosity and density ratio values. The results for $\lambda_\rho = 3$ at $Ca = 0.252$ are almost identical to

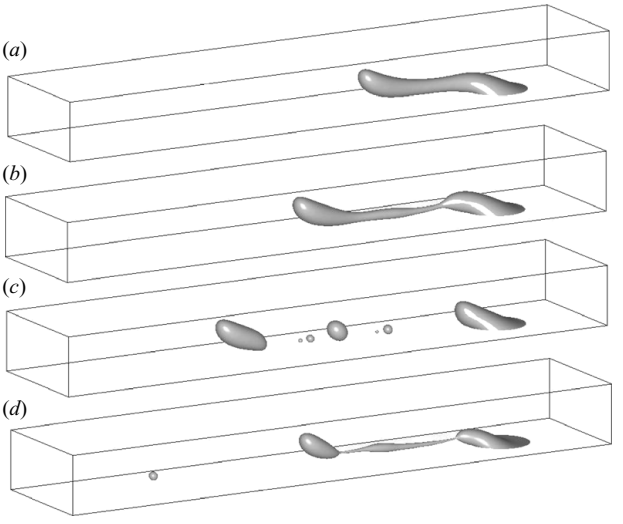

FIGURE 14. Snapshots of multiple breakups for a pinned droplet in shear flow at $Re = 45.3$ and $Ca = 0.194$ using $\Delta x = 0.0167$. From (*a*) to (*d*) is the sequence of events. Shear flow goes from right to left.

the dashed line in figure 13, whereas for $\lambda_\mu = 3$ the ligament was significantly longer at the point of pinch-off (not shown). The results for the largest value of λ_μ simulated ($= 10$) also show evidence of an onset of capillary instability, with the second neck rupturing first, but all other cases simulated have led to end-pinching, as in the 'rapid extension' regime observed by Marmottant & Villermaux (2004*b*) in the stretching of liquid ligaments. Although just beyond the critical condition for entrainment (i.e. at a relatively low value of Ca) only short ligaments are formed, a liquid 'column' (in the sense of 'rapid extension' regime of Marmottant & Villermaux 2004*b*) is still formed leading to end-pinching (see figure 16*a*). We have not observed a 'slow extension' regime (in the sense of Marmottant & Villermaux 2004*b*, in which a single rupture event occurs halfway down the ligament) in the cases studied here.

The behaviour at sufficiently large values of Ca is further complicated in that a second entrainment event may occur. An example of this behaviour is presented in figure 14, for $Re = 45.3$ and $Ca = 0.194$ for a pinned droplet (this also shows the breakup into multiple satellite droplets mentioned above; we have verified that doubling the grid spacing results in a very similar sequence, the only difference being that the two smallest satellite drops seen in figure 14*c* are then not resolved). Here, the 'mother' droplet remaining behind on the wall after the first entrainment event still has a relatively large volume (of an effective radius $r = 0.79$), resulting in a new flow configuration, i.e. $Ca = 0.154$ and $Re = 28.6$ which, as can be verified from figure 12, is still beyond criticality. A similar sequence of events was observed for a pinned droplet with $Ca = 0.252$ and $Re = 71.6$, where after the first entrainment the remaining droplet, with the new flow configuration $Ca = 0.20$ and $Re = 46.1$, underwent a second entrainment event. In principle, then, there is a critical condition beyond which multiple entrainment events occur, and we may even speculate about the existence of an entrainment 'cascade', at large values of Ca when more than two stages might occur, as in the droplet cascade of Thoroddsen & Takehara (2000). Since the simulation of many such stages (to allow for investigating whether the behaviour

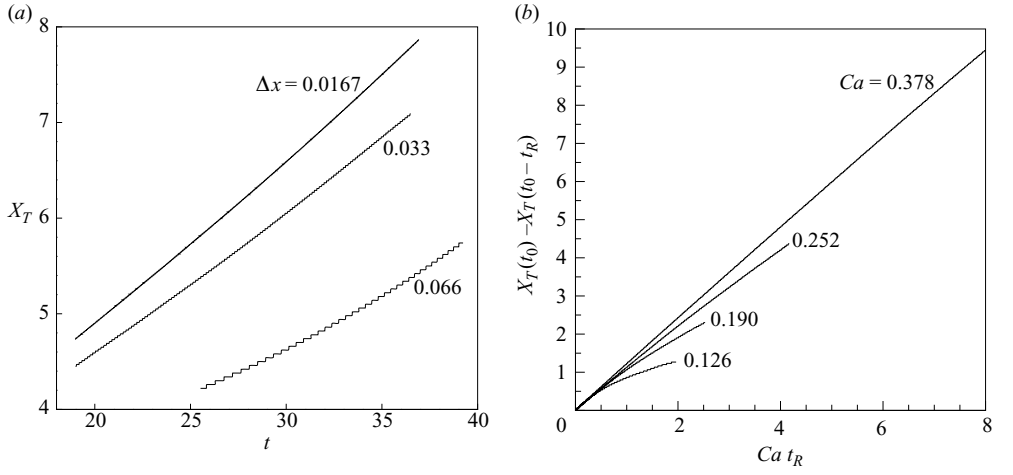

FIGURE 15. Ligament growth of a pinned droplet at $Re = 71.6$, $\lambda_\rho = 1$ and $\lambda_\mu = 1$. (*a*) Results of successively refined meshes at $Ca = 0.252$ keeping the CFL number constant, in terms of the x-position of the downstream tip of the ligament vs. time; (*b*) results for various Ca with a grid spacing of 0.033, in terms of relative ligament length vs. time to rupture.

is self-similar) would require an excessive computational effort, this is beyond the scope of this paper.

3.4. *Ligament dynamics*

Here, we investigate the rate of stretching of ligaments by the shear flow in terms of the streamwise position of the downstream tip of the ligament, $X_T(t)$. Results from various mesh spacings are shown in figure 15(*a*). The results appear to converge with refined mesh spacing. As can be seen from figure 15, the tip velocity is usually more or less constant, i.e. the ligament appears to be passively convected downstream (as observed for freely suspended drops in shear flow; see Cristini *et al.* 2003), but some acceleration is observed for relatively low values of Ca. The velocity of the tip was found to be strongly dependent on the value of Ca, however (note the scaled time axis used in figure 15*b*). Cristini *et al.* (2003) proposed that the length of freely suspended drops in an extensional flow increases linearly with time made dimensionless with the imposed shear rate, but this does not explain the sensitivity to the value of Ca observed in the present results. The passively convected ligament was also observed in a related problem, i.e. inviscid axisymmetric slender bubbles in an extensional flow (Booty & Siegel 2005). A different model has been proposed previously by Marmottant & Villermaux (2004*a*) for ligament growth on a gas-assisted jet. That model is based on a force balance over the ligament; it is an ordinary differential equation for the length of ligaments formed on a jet. In the model proposed by Marmottant & Villermaux (2004*a*), the inertial force exerted by the surrounding fluid is balanced by inertia of the ligament,

$$\frac{1}{2}\rho V_0 \frac{d^2\hat{L}}{d\hat{t}^2} \sim \frac{1}{2}\rho C_D S_0 U^2$$

where $\hat{L}$ is the ligament length, V_0 and S_0 are the initial ligament volume and cross-sectional surface area, respectively, C_D is a drag coefficient of the ligament, and U is the imposed velocity of the surrounding fluid.

But this appears not to be applicable to the conditions of the simulations reported here: the main force exerted by the surrounding fluid is a viscous contribution, and the rate of stretching is approximately constant, i.e. $\mathrm{d}^2X_T/\mathrm{d}t^2$ is rather small (we found that the streamwise position of the pinching neck changed on a much smaller scale in most cases, so the rate of change of a ligament length can be approximated by that of the value of X_T). Instead, the results are consistent with an energy balance wherein the force applied by the surrounding fluid is at least partly converted into surface energy,

$$\sigma \frac{\mathrm{d}}{\mathrm{d}\hat{t}} S_I \sim \int_{S_I} \boldsymbol{n} \cdot \boldsymbol{T} \cdot \boldsymbol{u} \, \mathrm{d}S. \tag{3.4}$$

The right-hand side of (3.4) scales as $\boldsymbol{T} \sim \mu\dot{\gamma}$, $\boldsymbol{u} \sim \dot{\gamma} R$ and $S \sim \dot{\gamma} R \hat{L}$, respectively; the left-hand side scales as $\sigma R \, \mathrm{d}\hat{L}/\mathrm{d}\hat{t}$. Hence, the inverse characteristic time scale for the rate of stretching is

$$\hat{L}^{-1} \, \mathrm{d}\hat{L}/\mathrm{d}\hat{t} \sim \mu\dot{\gamma}^2 R/\sigma = \dot{\gamma} Ca. \tag{3.5}$$

To facilitate a comparison with the numerical results, we define the following parameters: the dimensionless time to rupture $t_R \equiv t_0 - t$ and relative ligament length $L_R(t_R) \equiv (\hat{L}(t_0) - \hat{L}(t))/R \approx X_T(t_0) - X_T(t_0 - t_R)$, where t_0 is the time when the rupture of the ligament takes place and note $t \leqslant t_0$; $X_T(t_0)$ is the streamwise position of the downstream tip of the ligament at the instance of rupture. With these definitions we find from (3.5) that the time dependence of $X_T(t_0) - X_T(t_0 - t_R)$ is a function of $t_R Ca$ (evidently, assuming that the right-hand side of (3.5) is constant gives a linear relation). We have therefore plotted in figure 15(*b*) $X_T(t_0) - X_T(t_0 - t_R)$ versus $t_R Ca$. The results support the scaling argument. An inspection showed further that the result for $Ca = 0.126$ in figure 15(*b*) could be well represented by an exponential as suggested above. The results corresponding to figure 15(*b*) for a relatively low Reynolds number, $Re = 15.9$, were found to be very similar (not shown), with the exception of the largest value of $Ca = 0.378$, where a capillary-type instability was observed and pinching occurred first near the tip of the ligament. Tests show that the viscosity and density ratios have some, but no strong effect (see also figure 18*b*).

3.5. *Pinch-off*

Detailed views of the region where pinch-off first occurs are shown in figure 16. It can be seen in figure 16(*a*) that initially the ligament is the thinnest at a point (i.e. $x = X_M(t)$) that moves downstream, but that towards the final stages of the pinch-off process $X_M(t)$ moves upstream, consistent with the end-pinching in, for instance, droplet breakup in an extensional flow (e.g. Tjahjadi, Stone & Ottino 1992). Kang *et al.* (2005) observed a weak local maximum in the tangential stress in the 'neck' region and argued that this would drive the breakup. An extensional flow is seen to occur in figure 16(*b*), but the pressure distribution and associated flow inside the drop and ligament strongly suggest that these are curvature-dominated (certainly at this late stage of the pinch-off process).

Numerical simulations of pinch-off of a droplet dripping from a faucet (Notz & Basaran 2004) and experiments on a stretched ligament (Marmottant & Villermaux 2004*b*) have shown that a transition to the well-studied viscous–capillary pinch-off regime (see Eggers 1997; Lister & Stone 1998) occurs rather late in the process. Qualitatively, the shape of the pinching neck in figure 16(*a*) may appear to be approaching the results of Sierou & Lister (2003) for viscosity-matched fluids, but the slope of the cones on both sides of the pinching neck is still below that for the self-similar regime (e.g. the maximum slope of the large cone is approximately 1.5 in

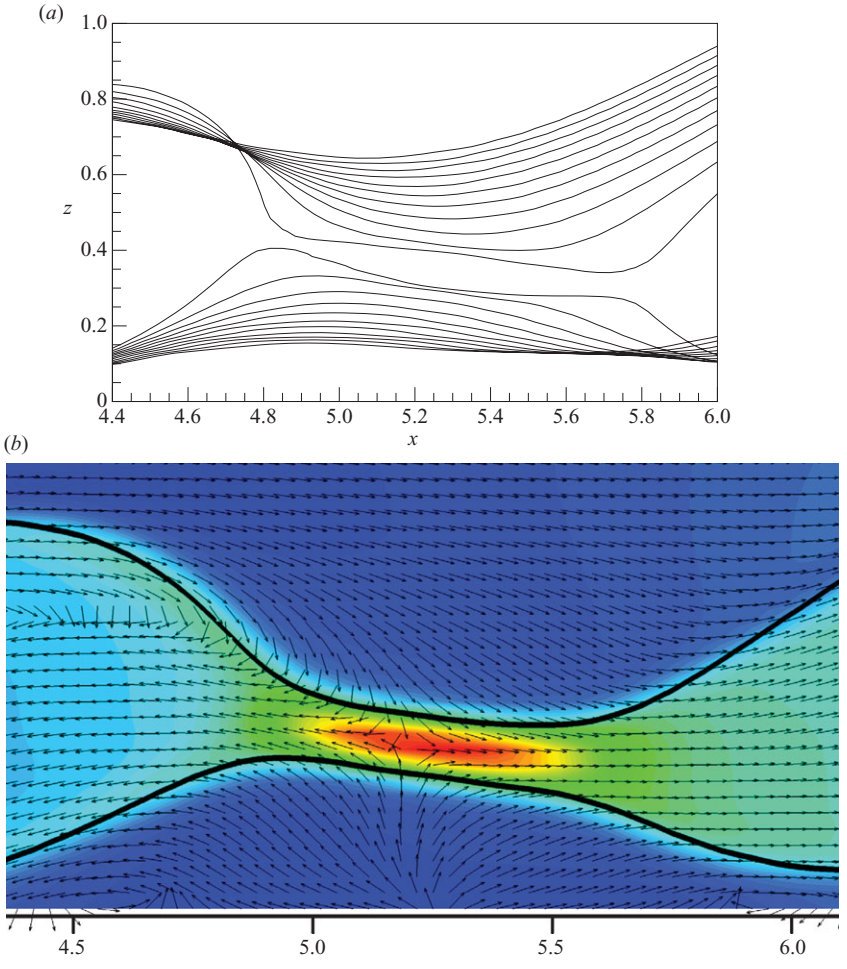

FIGURE 16. Zoomed view of the entrainment of a pinned droplet at $\lambda_\rho = 1$, $\lambda_\mu = 1$, $Re = 71.6$ and $Ca = 0.126$, showing (a) the ligament evolution with time and (b) the flow field before the rupture of the ligament in terms of pressure contour and velocity vectors, which are all of equal length and indicate the direction of the velocity only.

the final snapshot in figure 16, as opposed to about 5 in Sierou & Lister 2003). We would therefore expect a self-similar pinching regime to occur only just beyond the final snapshot shown in figure 16. More information on this issue is presented below, although the main aim here is to investigate the earlier behaviour of the entrainment process, which is the time during which the volume of entrained drops is primarily determined.

In figure 17(a) the minimum radius of the ligament r_{min} is plotted versus time to rupture $t_R \equiv t_0 - t$ on successively refined meshes, at $Re = 71.6$ and $Ca = 0.252$. The results appear to converge upon grid refinement. The values obtained for t_0 are 68.6, 65.3 and 61.6 when using $\Delta x = 0.0667$, 0.333 and 0.0167, respectively, which appears to converge approximately linearly with the grid spacing (especially since t_0 is reduced when the grid is refined, evidently suggesting a finite rupture time upon further grid refinement). Different choices of the time step upon grid refinement (either keeping

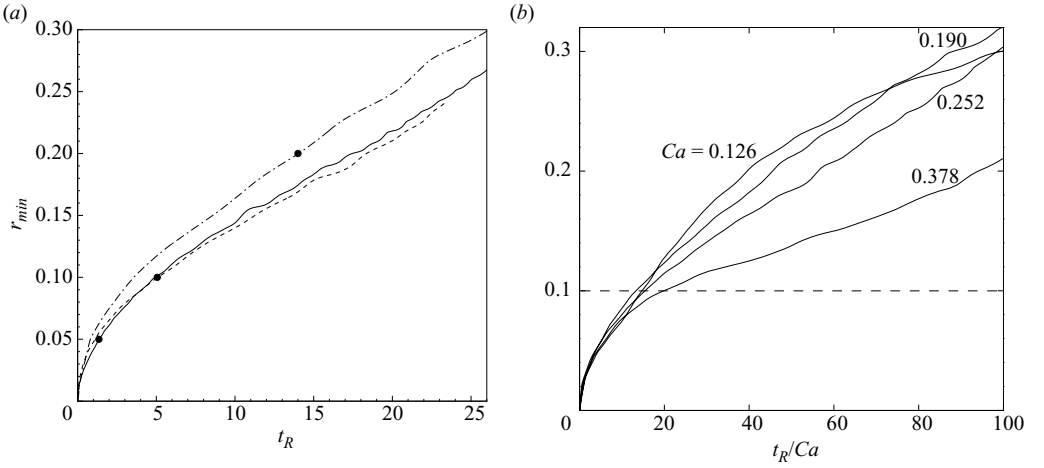

FIGURE 17. Radius of the pinching neck r_{min} vs. time to rupture for Case C at $Re = 71.6$, $\lambda_\rho = 1$ and $\lambda_\mu = 1$. (a) Convergence study for $Ca = 0.252$: solid line, $\Delta x = 0.0167$; dashed line, $\Delta x = 0.0333$; dash-dotted line, $\Delta x = 0.0667$; (b) r_{min} vs. t_R for the Ca values indicated, with $\Delta x = 0.0333$. Note that the numerical artefacts are expected to enter the pinch-off process when $r_{min} \leqslant 6\epsilon = 3\Delta x$, which is represented by dots in (a) and by the dashed line in (b).

a CFL number constant, or, as in the figure, the time step constant) resulted in the same trend.

In all cases, the results are similar in the sense that the minimum radius is approximately linear in the time to rupture, $t_R \equiv t_0 - t$, and then sharply changes with t_R when the rupture time t_0 is approached. The results for r_{min} were found to be especially sensitive to the value of Ca. To some extent this dependency can be captured, as has been done in figure 17(b), by making the time to rupture dimensionless with $R\mu/\sigma$ instead of the shear rate. This is what would be expected from a viscous self-similar regime (Lister & Stone 1998), but the three-dimensional motion and distortion of the ligament is too complex for a universal self-similar regime to have been approached at this stage. Also, as summarized in § 3.3, the approach to breakup is qualitatively very different even for the rather narrow range of values of Ca (one would also expect yet a different scaling to apply very close to pinch-off, from a self-similar regime; see Lister & Stone 1998). We have also obtained results for different Ca at a lower Reynolds number value ($Re = 15.9$) and found the trends to be similar (not shown).

Most of the slope transitions occur roughly at $r_{min} = 6\epsilon = 3\Delta x$, which represents the thickness of the diffuse interface between $C = 0.1$ and 0.9. In principle, it is anticipated that the dynamics beyond that stage are affected by the finite thickness of the interface. But the result for the finest grid in figure 17(a) shows a change in slope before this point is reached, and we may speculate that a transition to an asymptotic regime may be approached at this very late stage of the pinch-off process. A close inspection of these results has shown that the change of behaviour of r_{min} more or less coincides with the reversal of the motion of the position of the pinching neck, more precisely, from moving downstream to moving upstream. Further grid refinement proved impossible due to memory limitations. In any event, a monotonic convergence has been achieved in terms of the rupture time t_0. Furthermore, the slopes of the curves in the linear regime in figure 17(a) are very close, regardless of the difference in grid spacing. In this respect, very similar results were found for

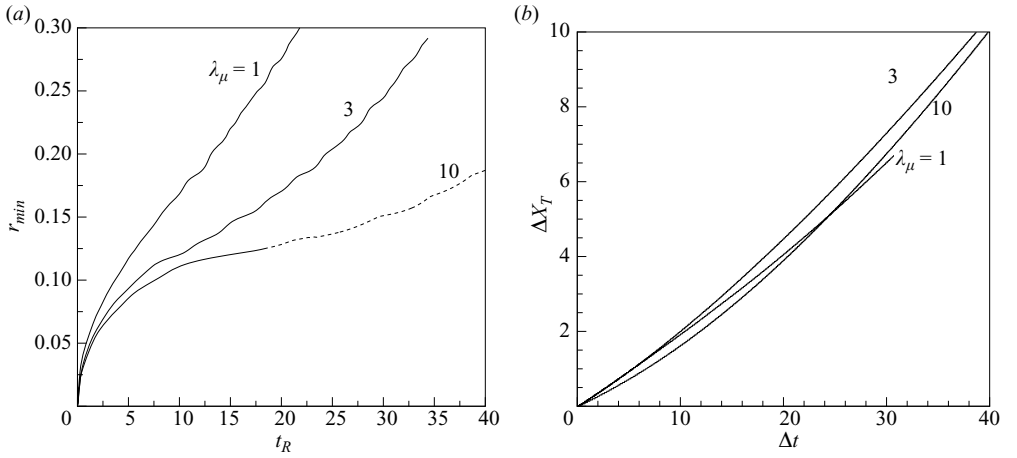

FIGURE 18. Effect of viscosity ratio on the minimum radius (a) and the x-position of the downstream tip of the ligament vs. time. $Re = 71.6$, $Ca = 0.252$, $\lambda_\rho = 1$ and grid spacing 0.033. The significance of the dashed line section in (a) is explained in the text. In (b), $\Delta X_T = X_T - 6.0167$ and $\Delta t = t - t(X_T = 6.0167)$.

different values of density ratios, e.g. $\lambda_\rho = 3$ and 10, only the slope for $\lambda_\rho = 10$ being somewhat lower.

The results are also sensitive to the value of the viscosity ratio; see figure 18(a). Increasing λ_μ leads to a delay in the onset of the final pinch-off stages. During such delays the ligament continues to be stretched, culminating in several pinching regions, at $\lambda_\mu = 10$. In fact, at $\lambda_\mu = 10$ two necks were formed and simultaneously developed during the ligament stretching. The minimum ligament radius is initially at the first site downstream from the mother droplet and then switches to the second site just before pinch-off. Since our code tracks the instantaneous minimum radius of the entire ligament, we distinguish these two different stages in figure 18 by using a dashed and solid line segment, respectively.

3.6. *Breakup or detachment of a sliding droplet*

We investigate here the occurrence of pinch-off or detachment for a moving droplet. From the study in the previous sections, both sliding and entrainment events are expected to play important roles. These two trends may compete with each other: on the one hand, the formation and growth of a ligament is a prerequisite for the occurrence of pinch-off, as shown in § 3.2; on the other hand, the ligament formation implies an increasing value of θ_m, and consequently leads to a faster contact-line speed (see figure 9). This in turn would hinder further ligament growth because a reduction in velocity at the drop height of the oncoming shear flow and the drop velocity may expect to effectively reduce the shear stress on the droplet. The initial condition for especially the velocity field may play an important role in this respect, and we stress that the results in this section are for the same initial conditions as stated in § 2.1.

Figure 19 shows the critical condition for the onset of entrainment for a moving droplet, in terms of Ca_c as a function of Re for Cases A and D, together with the corresponding critical values for the onset of motion in Ding & Spelt (2008) (in that work, a different length scale was used, the previous results shown here for comparison have been rescaled accordingly). It is seen that for Case A, Ca_c at the onset of entrainment is almost constant (≈ 0.32) for $Re < 130$, and decreases

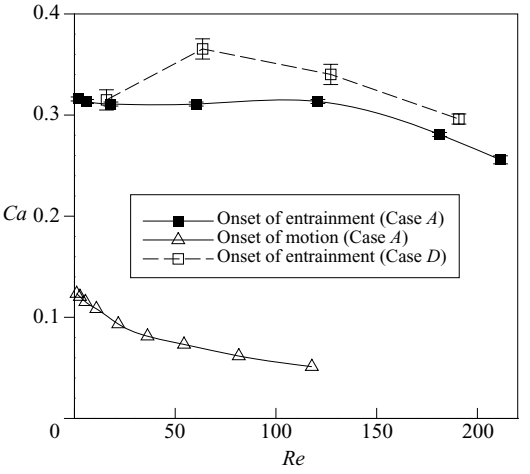

FIGURE 19. Critical conditions of the onset of entrainment for a sliding droplet in terms of the critical capillary number as a function of Reynolds number. The upper bound of the error bar represents the lowest Ca at which the entrainment occurs in the simulation, whereas the lower bound represents the highest Ca at which no entrainment is observed.

when $Re > 130$, in which regime inertial effects are expected to become significant. It is naturally seen that Ca_c for the onset of entrainment is generally larger than its counterpart for the onset of motion (such that there is the clearly defined flow regime of quasi-steadily moving drops investigated in § 3.1). In addition, from figure 19 we can see that Case D generally requires a larger Ca than Case A for entrainment at all Reynolds numbers. With the same θ_A but a smaller hysteresis window, the droplet experiences less resistance forces arising from contact-angle hysteresis in Case D than in Case A, and thus a faster contact-line speed is expected in Case D at the same Ca. To compensate the decrease of shear stress exerted on the drop due to fast contact-line motion, a larger Ca is then needed for the occurrence of drop entrainment. Also, Ca_c of a moving droplet is larger than the value required for a pinned droplet (see figure 12). When evaluating (3.2) at criticality, Ca_c increases linearly with Ca_{cl} when ignoring inertial effects. This argument has been shown previously to partly explain the differences between Ca_c for entrainment of pinned and moving drops for the two-dimensional system (Spelt 2006). But, of course, it ignores any changes in the shape of drops for different flow conditions and, indeed, the change in shape due to the fixed window of contact-angle hysteresis. Because of numerical limitations, the effective slip length in these simulations is too large for direct comparison with experiment, so droplets move more easily in the numerical simulation than those in experiment, and one might expect experimental critical capillary number values to lie between those shown in figures 12 and 19.

Two typical three-dimensional views at criticality for pinch-off are shown in figure 20, at low ($Re = 1.8$ and $Ca = 0.32$) and moderate ($Re = 180$ and $Ca = 0.28$) Reynolds numbers, respectively. The velocity field at the cross-section for a droplet just above the onset of entrainment at $Re = 18$ is shown in figure 21(a), which has similar wake structures to the two-dimensional results obtained by Spelt (2006) at $Re = 10$. Below the onset of entrainment, the wake structure behind a steadily moving droplet at $Re = 211.5$ appears to be similar to the one behind a stationary droplet observed by Ding & Spelt (2008), as shown in figure 21(b).

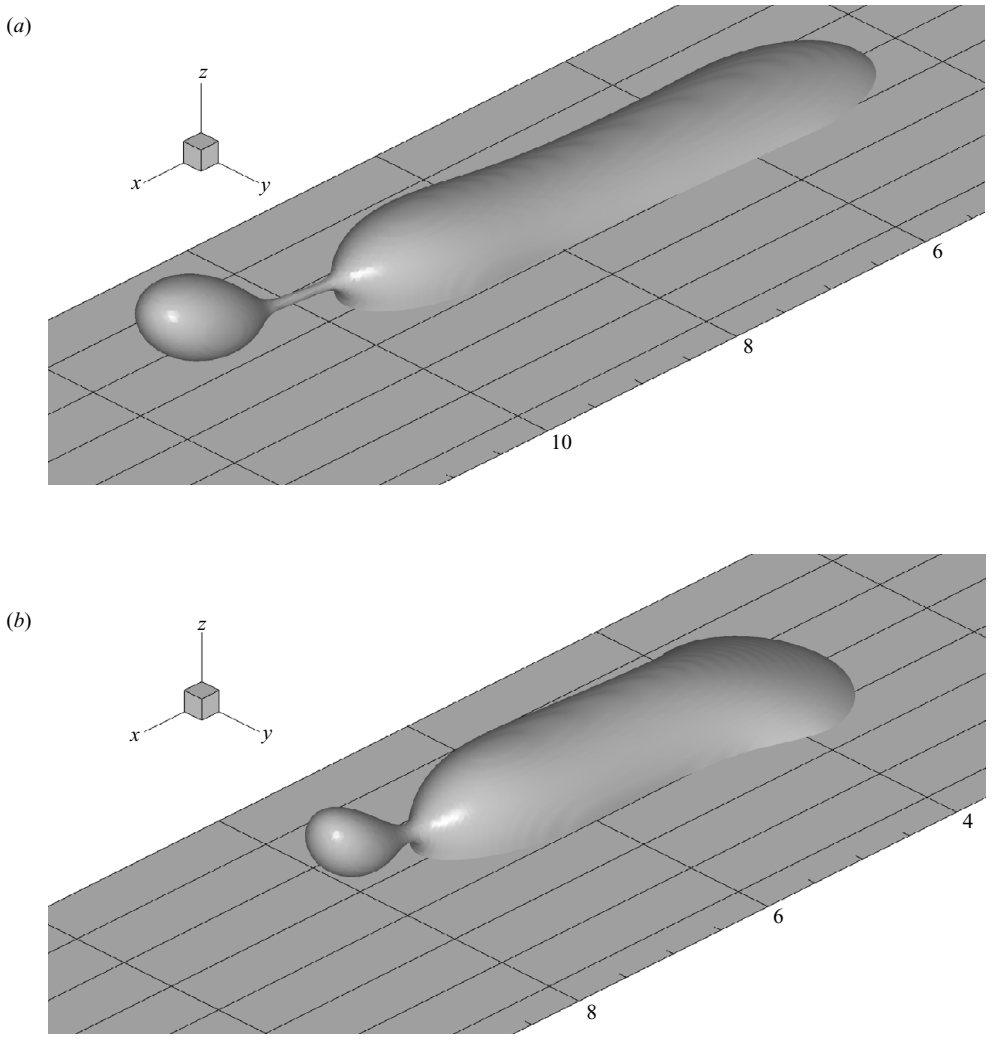

FIGURE 20. Three-dimensional view of the droplet at criticality for Case A. (a) $Re = 1.8$ and $Ca = 0.321$, (b) $Re = 180$ and $Ca = 0.28$.

Droplet entrainment is a dynamic combination of a number of physical processes. Apart from the shear flow rate, there are other factors, such as slip length and the initial configuration, that may also affect the onset of entrainment for a moving droplet. Figure 22 shows an indication of the effect of slip length by comparing results for dimensionless slip length values of 0.03 and 0.045, at $Re = 18$ and $Ca = 0.32$. We can see that drop entrainment happens for the case with a slip length of 0.03 but is not observed for the larger slip length value. It has been shown by Ding & Spelt (2008) that the effect of slip length on the sliding process seems to primarily affect the dynamic behaviour of the droplet sliding. In other words, a small slip length tends to result in a smaller transient contact-line speed than a large slip length. It is seen in figure 22 that the upstream part of the contact line moves at a faster speed in the case of $\lambda/R = 0.045$ than that in the case of $\lambda/R = 0.03$, effectively holding back the top of the droplet and preventing the droplet from pinching-off. The initial configuration may also influence the pinch-off process. We find that drop entrainment does not

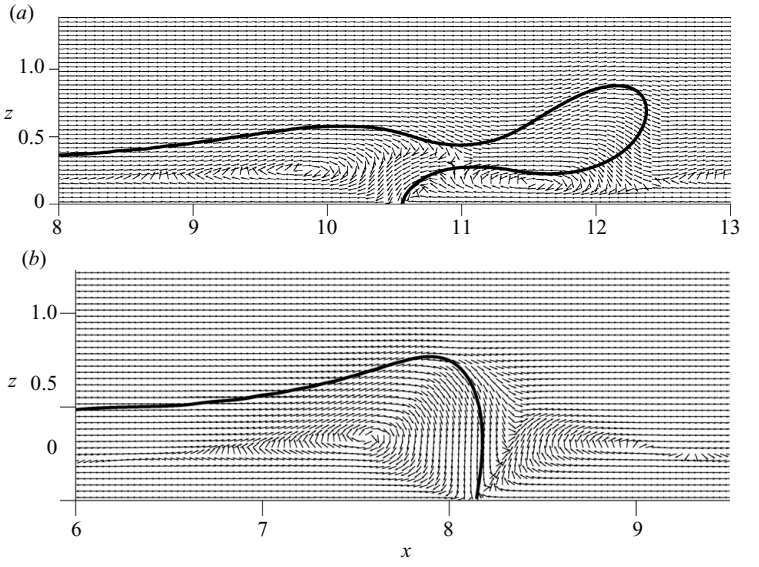

FIGURE 21. Velocity vectors at cross-sections for droplets of Case *A*, i.e. (x,z) plane at $y=0.0167$, with $\lambda_\mu=\lambda_\rho=1$. (*a*) $Re=18$ and $Ca=0.32$, (*b*) $Re=211.5$ and $Ca=0.252$. The velocity vectors have been rescaled by subtracting the advancing speed of the droplet at the downstream end.

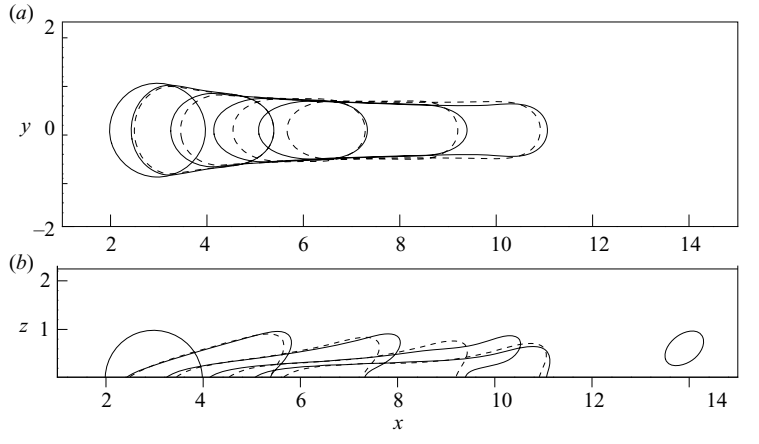

FIGURE 22. Effects of slip length on the drop entrainment of moving droplets with an initial configuration of Case *A*. Successive snapshots of droplets in the cross-section at successive times of a regular interval at $Re=18$ and $Ca=0.32$. Solid lines represent results with a slip length of 0.03, while dashed lines represent results with a slip length of 0.045. Contact lines (*a*) and cross-section (*b*).

occur in our numerical experiments for Case *B* whereas it did for Case *A*, for $Re=18$, $Ca=0.32$ and a slip length of 0.03.

We conclude this section with an investigation into the entrainment of a hydrophobic droplet, with a contact-angle hysteresis of $\theta_A=140^\circ$ and $\theta_R=90^\circ$ and an initial contact angle of 90°. Figure 23 shows two typical regimes observed in the cases investigated for the entrainment of a hydrophobic droplet: pinch-off and detachment. It is expected that the detachment of a hydrophobic droplet is similar to the physical

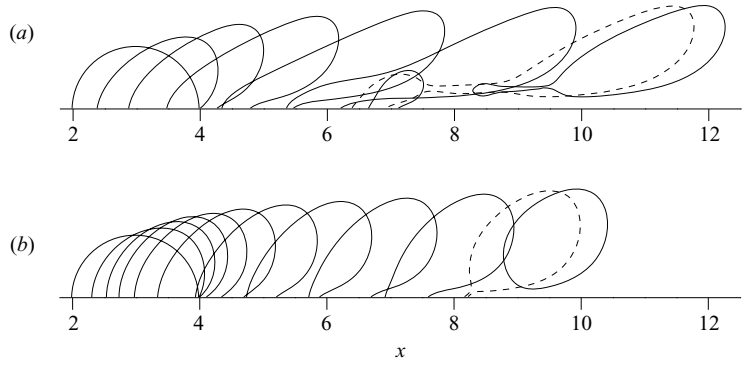

FIGURE 23. Snapshots of the droplet for the case $\theta_A = 140°$, $\theta_A = 90°$ and $\theta_0 = 90°$, at $Re = 18$. Solid lines represent the solutions at successive times of a regular interval (*a*) $Ca = 0.096$ and (*b*) $Ca = 0.046$. Dashed line represents the solutions at the onset of entrainment or detachment.

process in shear flow past a rigid sphere on a solid wall (Bagchi & Balachandar 2002). Viscous and inertial forces exerted on the surface of the droplet generate a hydrodynamic torque, leading to the rotation of the droplet before the pinch-off. We can also see that a larger portion of the droplet breaks off at the top as a result of the increased window of contact-angle hysteresis. In our numerical simulations two features are distinct from the entrainment of hydrophilic droplets, which we mostly considered in this paper: it is much easier to generate entrainment/detachment for hydrophobic droplets than hydrophilic regarding the magnitude of shear flow rate, and the detachment regime is not observed for hydrophilic droplets.

4. Conclusions

A diffuse-interface method has been used to study the motion and continuous deformation of a three-dimensional droplet on a solid surface in a suddenly applied shear flow. Properties of continuously sliding drops have been investigated in detail. Some results confirmed the relevance of findings for the corresponding two-dimensional problem (Spelt 2006), such as the relation between θ_m and the instantaneous contact-line speed; on the other hand, the present results show a smaller role of inertial effects in the critical condition for the onset of entrainment, both for pinned and moving drops.

Some effort was put in the model development of the entrainment process. It was found that the length of a ligament increases more or less linear with time on a time scale $\sigma/(\mu\dot{\gamma}^2 R)$, which could be explained using an energy argument. This ligament growth is suddenly terminated when pinching occurs. Ligaments were found to elongate to very substantial lengths when Ca or λ_μ was increased. It was found that the radius of a pinching neck changes approximately on a time scale $R\mu/\sigma$, although many of such time units would be required for pinch-off to take place. A further issue here is that the type of breakup changes rapidly with the value of Ca, with capillary breakup appearing to approach relatively close to the conditions for entrainment.

Because of the limitation of computational resources, the effective slip length in our simulations is larger than that encountered in experimental conditions, by several orders of magnitude. As shown in figure 22, the slip length affects the occurrence of pinch-off for a sliding droplet. On the other hand, the effective slip length could be

varied in the present paper to such an extent that it could determine whether or not entrainment would occur. Also, a local maximum angle between the interface and the wall was found to be primarily determined by the value of a capillary number based on the instantaneous contact-line speed. The results obtained so far suggest that contact-line motion of a droplet driven by shear is rather different from that of conventional spreading. More work is required (e.g. using adaptive grid refinement methods) to assess to what extent this remains the case for much smaller values of an effective slip length.

The authors would like to acknowledge financial support from EPSRC under grant numbers EP/D031222 and EP/E046029/1.

REFERENCES

Bagchi, P. & Balachandar, S. 2002 Shear versus vortex-induced lift force on a rigid sphere at moderate *Re*. *J. Fluid Mech.* **473**, 379–388.

Booty, M. R. & Siegel, M. 2005 Steady deformation and tip-streaming of a slender bubble with surfactant in an extensional flow. *J. Fluid Mech.* **544**, 243–275.

Chatterjee, J. 2001 A criterion for buoyancy induced drop detachment based on an analytical approximation of the drop shape. *Coll. Surf. A: Physiochem. Engng Asp.* **178**, 249–263.

Cristini, V., Guido, S., Alfani, A., Blawzdziewicz, J. & Loewenberg, M. 2003 Drop breakup and fragment size distribution in shear flow. *J. Rheol.* **47**, 1283–1298.

Cox, R. G. 1986 The dynamics of the spreading of liquids on a solid surface. Part 1. Viscous flow. *J. Fluid Mech.* **168**, 169–194.

Dimitrakopoulos, P 2007*a* Deformation of a droplet adhering to a solid surface in shear flow: onset of interfacial sliding. *J. Fluid Mech.* **435**, 327–350.

Dimitrakopoulos, P 2007*b* Gravitational effects on the deformation of a droplet adhering to a horizontal solid surface in shear flow. *Phys. Fluids* **19**, 122105.

Dimitrakopoulos, P. & Higdon, J. J. L. 1998 On the displacement of three-dimensional fluid droplets from solid surfaces in low-Reynolds-number shear flows. *J. Fluid Mech.* **377**, 189–222.

Ding, H. & Spelt, P. D. M. 2007*a* Inertial effects in droplet spreading: a comparison between diffuse interface and level-set simulations. *J. Fluid Mech.* **576**, 287–296.

Ding, H. & Spelt, P. D. M. 2007*b* Wetting condition in diffuse interface simulation of contact line motion. *Phys. Rev.* E **75**, 046708.

Ding, H. & Spelt, P. D. M. 2008 Onset of motion of a three-dimensional droplet on a wall in shear flow at moderate Reynolds numbers. *J. Fluid Mech.* **599**, 341–362.

Ding, H., Spelt, P. D. M. & Shu, C. 2007 Diffuse interface model for incompressible two-phase flows with large density ratios. *J. Comput. Phys.* **226**, 2078–2095.

Dussan V., E. B. 1987 On the ability of drops to stick to surfaces of solids. Part 3. The influences of the motion of the surrounding fluid on dislodging drops. *J. Fluid Mech.* **174**, 381–397.

Dussan V., E. B. & Chow, R. T. P. 1983 On the ability of drops or bubbles to stick to non-horizontal surfaces of solids. *J. Fluid Mech.* **137**, 1–29.

Eames, I., Gilbertson, M. A. & Landeryou, M. 2005 The effect of an ambient flow on the spreading of a viscous gravity current. *J. Fluid Mech.* **523**, 261–275.

Eggers, J. 1997 Nonlinear dynamics and breakup of free-surface flows. *Rev. Mod. Phys.* **69**, 865–929.

Golpaygan, A. & Ashgriz, N. 2008 Multiphase flow model to study channel flow dynamics of PEM fuel cells: deformation and detachment of water droplets. *Intl J. Comput. Fluid Dyn.* **22**, 85–95.

Hodges, S. R. & Jensen, O. E. 2002 Spreading and peeling dynamics in a model of cell adhesion. *J. Fluid Mech.* **460**, 381–409.

Jacqmin, D. 2000 Contact-line dynamics of a diffuse fluid interface. *J. Fluid Mech.* **402**, 57–88.

Kang, Q., Zhang, D. & Chen, S. 2005 Displacement of a three-dimensional immiscible droplet in a duct. *J. Fluid Mech.* **545**, 41–66.

Khismatullin *et al.* 2003 Inertia-induced breakup of highly viscous drops subjected to simple shear. *Phys. Fluids* **15**, 1351–1354.

Le Grand, N., Daerr, A. & Limat, L. 2005 Shape and motion of drops sliding down an inclined plane. *J. Fluid Mech.* **541**, 293–315.

Lister, J. R. & Stone, H. A. 1998 Capillary breakup of a viscous thread surrounded by another viscous fluid. *Phys. Fluids* **10**, 2758–2764.

Marmottant, P. & Villermaux, E. 2004*a* On spray formation. *J. Fluid Mech.* **498**, 73–112.

Marmottant, P. & Villermaux, E. 2004*b* Fragmentation of stretched liquid ligaments. *Phys. Fluids* **16**, 2732–2741 and Erratum: **18**, 059901–1.

Notz, P. K. & Basaran, O. A. 2004 Dynamics and breakup of a contracting liquid filament. *J. Fluid Mech.* **512**, 223–256.

Pan, L. & Hanratty, T. J. 2002 Correlation of entrainment for annular flow in horizontal pipes. *Intl J. Multiph. Flow* **28**, 385–408.

Rallison, J. M. 1984 The deformation of small drops and bubbles in shear flows. *Annu. Rev. Fluid Mech.* **16**, 45–66.

Rio, E., Daerr, A., Andreotti, B. & Limat, L. 2005 Boundary conditions in the vicinity of a dynamic contact line: experimental investigation of viscous drops sliding down an inclined plane. *Phys. Rev. Lett.* **94**, 024503.

Schleizer, A. D. & Bonnecaze, R. T. 1999 Displacement of a two-dimensional immiscible droplet adhering to a wall in shear and pressure-driven flows. *J. Fluid Mech.* **383**, 29–54.

Sierou, A. & Lister, J. R. 2003 Self-similar solutions for the viscous capillary pinch-off. *J. Fluid Mech.* **497**, 381–403.

Spelt, P. D. M. 2006 Shear flow past two-dimensional droplets pinned or moving on an adhering channel wall at moderate Reynolds numbers: a numerical study. *J. Fluid Mech.* **561**, 439–463.

Sugiyama, K. & Sbragaglia, M. 2008 Linear shear flow past a hemispherical droplet adhering to a solid surface. *J. Engng Math.* **62**, 35–55.

Thiele, U. & Knobloch, E. 2006 On the depinning of a driven drop on a heterogeneous substrate. *New J. Phys.* **8**, 1–37.

Thoroddsen, S. T. & Takehara, K. 2000 The coalescence cascade of a drop. *Phys. Fluids* **12**, 1265–1267.

Tjahjadi, M., Stone, H. A. & Ottino, J. M. 1992 Satellite and subsatellite formation in capillary breakup. *J. Fluid Mech.* **243**, 297–317.